

# SAGAN-VI: When Jets Meet Filaments – Environmental Imprints on the Growth of Giant Radio Galaxies

Mousumi Mahato<sup>1\*</sup>, Elmo Tempel<sup>1</sup>, Shishir Sankhyayan<sup>1</sup>, Pratik Dabhad<sup>2</sup>, and Kshitij Chavan<sup>3</sup>

<sup>1</sup>Tartu Observatory, University of Tartu, Observatooriumi 1, 61602 Tõravere, Estonia

<sup>2</sup>Astrophysics Division, National Centre for Nuclear Research, Pasteura 7, 02-093 Warsaw, Poland

<sup>3</sup>Inter-University Centre for Astronomy and Astrophysics (IUCAA), Pune 411007, India

December 10, 2025

## ABSTRACT

**Context.** Giant radio galaxies (GRGs) represent the largest individual astrophysical structures, rivalling galaxy clusters in physical extent. Understanding how they attain such scales demands examining their large-scale cosmic surroundings, particularly the under-explored filament environment.

**Aims.** We quantify the three-dimensional (3D) distance of GRGs from the nearest filament spine; test how this distance correlates with their growth and formation of different morphological classes; assess whether their radio jets exhibit preferred orientations relative to filament axes; and examine how filament anisotropy from spine-to-periphery modulates radio morphology.

**Methods.** We employed a filament catalogue from the Sloan Digital Sky Survey (SDSS) together with the largest GRG catalogue currently available. For each source, we measured the comoving distance to the nearest filament spine, the projected jet-spine orientation angle, and quantified lobe asymmetry via the arm-length ratio (ALR). These metrics trace proximity, directionality, and the impact of filamentary environment on morphology. We then compared GRGs with a control sample of small radio galaxies (SRGs) to constrain the environmental factors that regulate the attainment of giant sizes. We validated the robustness of our results via bootstrap resampling and non-parametric statistical tests.

**Results.** Our results show that GRGs and SRGs have similar filament occupancy. By contrast, GRGs preferentially display larger alignment angles relative to filament spines, while SRG orientations are consistent with a random distribution. GRGs further show enhanced morphological asymmetry, reflected in lower ALR values than SRGs.

**Conclusions.** Attainment of giant sizes is not governed by proximity to filaments; rather, it correlates with jet-filament alignment. GRGs are preferentially oriented at large angles to filament spines, consistent with the propagation of jets through lower-density void-facing channels that minimise environmental resistance. Consistently, lobe asymmetry mirrors this alignment, indicating that GRGs experience steeper transverse spine-to-void differential ram-pressure gradients along their paths.

**Key words.** galaxies: active – galaxies: jets – radio continuum: galaxies – galaxies: large-scale structure: filaments.

## 1. Introduction

Powerful radio galaxies (RGs) drive magnetised, collimated, relativistic jets (Blandford et al. 2019) into the intergalactic medium (IGM), making them exquisitely sensitive, spatially extended probes of galaxy-environment coupling from tens of kiloparsecs (kpc) to several megaparsecs (Mpc). In the canonical Fanaroff-Riley framework, collimated, relativistic FRII jets terminate in compact hotspots and inflate synchrotron-bright lobes, whereas jets that decelerate more gradually produce edge-darkened, diffuse FRI structures (Fanaroff & Riley 1974). RGs can be further classified based on their projected linear sizes: giant radio galaxies (GRGs) are systems with sizes exceeding 0.7 Mpc, and small radio galaxies (SRGs) have sizes below 0.7 Mpc. GRGs (for review, see; Dabhad<sup>2</sup> et al. 2023) with their extreme sizes mark the ultimate stage of growth of RGs, and therefore, are natural laboratories for testing how ambient density, pressure, and magnetisation modulate jet propagation and lobe evolution. Born in the host galaxy, the GRG jets propagate through the IGM, and eventually emerge onto the scales of the cosmic web; en route, they encounter a variety of environments whose

influences are imprinted in the form of lobe-size and flux-density asymmetries, altered collimation and depolarisation patterns, as well as in signatures of episodic nuclear activity (e.g., Dabhad<sup>2</sup> et al. 2025). Decoding these diagnostics will help identify the physical conditions that permit their growth to Mpc scales.

Since the pioneering discovery of GRGs 3C236 and DA240 by Willis et al. (1974) to the recent and largest one, *Porphyron* ( $\sim 7$  Mpc) by Oei et al. (2024), the radio telescopes, with improving resolution, sensitivity and sky coverage, have catalogued nearly 12000 GRGs (e.g., Mostert et al. 2024) till now. Yet, despite this progress, GRGs appear to be relatively rarer compared to SRGs. The extraordinary sizes of GRGs are generally attributed to three main scenarios. First, they may be powered by exceptionally powerful and long-lived AGN activity, driving jets to large distances (e.g., Gopal-Krishna et al. 1989; Wiita et al. 1989; Dabhad<sup>2</sup> et al. 2020a). Second, their growth could result from recurrent or episodic jet activity, where multiple cycles of outbursts extend the lobes over time (Dabhad<sup>2</sup> et al. 2025). Third, GRGs are often found in relatively low-density environments, where the reduced external pressure allows jets to propagate farther without significant disruption (e.g., Mack et al. 1998; Malarecki et al. 2015; Stuardi et al. 2020).

\* E-mail: mousumi.mahato@ut.ee

Both [Casadei et al. \(2024\)](#) and [Massaro et al. \(2019\)](#) show that RGs, regardless of morphology (FRI or FRII) or optical excitation class (low or high), occupy a wide variety of environments ranging from poor groups to rich clusters, with no statistically significant difference in environmental richness between these categories. Their results consistently indicate that radio morphology and excitation type are not primarily governed by the large-scale environment at low redshift. The main distinction lies in their methods: [Casadei et al. \(2024\)](#) used photometric red-sequence galaxy counts within 0.5 Mpc of each radio galaxy, probing the inner cluster regions, while [Massaro et al. \(2019\)](#) used spectroscopic neighbour counts within 2 Mpc, characterising the broader group and cluster environments. Despite these differences in scale and sample selection (bright 3CR sources in comparison with the more homogeneous FRI and FRII samples), both studies reach the same conclusion that the surrounding environment plays only a secondary role, while intrinsic factors such as host galaxy properties and AGN power are the dominant influences on radio morphology and activity. Similarly, focusing specifically on GRGs, [Lan & Prochaska \(2021\)](#) examined 110 GRGs and found no correlation between their sizes and local galaxy density or distance to large-scale filaments. Their results show that GRGs inhabit environments comparable to those of SRGs, suggesting that the growth of radio structures is driven primarily by intrinsic factors rather than external environmental conditions.

Studies by [Dabhade et al. \(2020b,a\)](#) first showed that around 10-20% of GRGs are located at the centres of galaxy clusters, posing a challenge to the primary hypothesis that GRGs preferentially grow in low-density environments. A recent localisation of luminous GRGs within Bayesian reconstructions of the cosmic web ([Oei et al. 2024](#)) sharpens this picture by revealing that giants prefer denser structures akin to RGs in general, consistent with a radio-luminosity-density relation in which powerful jets preferentially occur in dense environments. Based on their analysis, around  $\sim 24\%$  of giants inhabit galaxy clusters, and for  $\sim 60\%$  of GRGs, the most probable environment is filament with negligible void occupancy. Complementary work by [Sankhyayan & Dabhade \(2024\)](#) finds that  $\sim 24\%$  of GRGs are cluster-associated, with  $\sim 5\%$  of them in superclusters. They also highlight that the largest GRGs ( $\gtrsim 3$  Mpc) grow in sparse environments. Moreover, case studies of the largest giants: *Alcyoneus* ( $\sim 5$  Mpc) and *Porphyron* ( $\sim 7$  Mpc) reveal that they are likely growing within cosmic filaments ([Oei et al. 2022; Oei et al. 2024](#)), yet the lobes of *Porphyron* are penetrating cosmic voids with a high probability. *Porphyron*, in particular, exemplifies how powerful radio outflows can arise from dense filaments and channel energy far into low-density volumes.

As part of the Search and analysis of giant radio galaxies with associated nuclei (SAGAN) project<sup>1</sup> ([Dabhade et al. 2020a](#)), we aim to investigate how the large-scale, filamentary structure of the cosmic web influences the growth and evolution of GRGs. Specifically, we examine the role of the less well-characterised cosmic web filaments in shaping their morphology and evolutionary pathways. These filaments are the Universe's intricate, grand architecture, woven from galaxies, gas, and dark matter, stretching across several megaparsecs. Serving as cosmic bridges between galaxy groups and clusters, they channel gas into galaxies, fuel star formation and drive galaxy evolution. The advent of wide, highly sensitive radio surveys together with deep optical data now makes it possible to investigate environments in unprecedented detail, allowing us to precisely localise

radio galaxies within cosmic filaments, probe their interactions, and address key questions such as:

- whether there is any difference in occupancy of GRGs and SRGs in filaments;
- how three-dimensional (3D) distance from filaments relates to morphology and projected linear sizes;
- whether radio-jet axes exhibit preferential alignment with local filament, and whether this preference differs between SRGs and GRGs;
- whether filaments imprint morphological asymmetries in SRGs and GRGs, and how these signatures compare across the two populations.

All these aspects are very significant to identify any distinctive pattern of interactions of SRGs and GRGs with filament environments, thereby unveiling how cosmic filaments - the principal habitat of GRGs, mediate jet propagation and ultimately regulate their growth and evolution.

The outline of the paper is as follows: In Sec. 2 we describe the construction of GRG, SRG samples and the filament catalogue. Sec. 3 and the subsections therein detail the methods and statistical framework employed for a comprehensive comparative study. This is followed by our results in Sec. 4. Sec. 5 interpret these findings and discusses their implications, and Sec. 6 summarises the main conclusions and outlines future prospects.

The flat  $\Lambda$  cold dark matter cosmological model has been adopted throughout this paper, based on the Planck results ( $H_0 = 67.8 \text{ km s}^{-1} \text{ Mpc}^{-1}$ ,  $\Omega_m = 0.308$ , and  $\Omega_\Lambda = 0.692$ ; [Planck Collaboration et al. 2016](#)). The images are presented in the J2000 coordinate system.

## 2. Data and sample selection

The first subsection is dedicated to detailing the filament catalogue utilised in this study. The subsequent subsections give a detailed account of the procedures used to construct the GRG and SRG samples.

### 2.1. The filament catalogue

[Tempel et al. \(2014\)](#) constructed a comprehensive catalogue of filamentary structures in the cosmic web by analysing the spatial distribution of galaxies from the Sloan Digital Sky Survey Data Release 8 (SDSS; [York et al. 2000](#), [Aihara et al. 2011](#)). The dataset with redshifts accurate to  $\sim 30 \text{ km s}^{-1}$ , was restricted to galaxies with r-band apparent magnitudes  $m_r = 17.77$  within the redshift range  $0.009 < z \leq 0.155$ . This selection ensured both spectroscopic completeness and a sufficiently dense sampling for filament detection.

The filament identification in [Tempel et al. \(2014\)](#) was carried out using the Bisous model (for details, see [Stoica et al. 2005](#); [Tempel et al. 2016](#)), a statistically rigorous filament-finding algorithm based on marked point processes with interactions. In this approach, the cosmic web is represented as a network of small cylindrical segments that collectively trace elongated overdensities in the galaxy distribution. Each cylinder, with a characteristic radius of  $\sim 0.5 h^{-1} \text{ Mpc}$ , acts as a local filament element; their alignment and connectivity are optimised within a Bayesian framework to maximise consistency with the observed galaxy positions. The model employs Markov Chain Monte Carlo sampling to explore filament configurations and generates a three-dimensional probability field describing the filamentary network. From this field, filament spines and local orientation vectors are extracted with sub-megaparsec precision.

<sup>1</sup> <https://sites.google.com/site/anantasakyatta/sagan>

Unlike many other filament-finding methods, the Bisous model does not require a smoothed density field, predefined nodes, or assumptions about galaxy luminosity or mass. It works directly with galaxy positions, allowing detection of both strong and weak filaments while remaining robust to survey limitations. Accordingly, the [Tempel et al. \(2014\)](#) catalogue provides a statistically robust and morphologically accurate mapping of the filamentary network, making it particularly well suited for localising RGs within their large-scale environments.

## 2.2. The GRG sample

To investigate the properties of GRGs within the cosmic web filaments, we compiled a sample of sources lying within the sky coverage of SDSS filaments (Sec. 2.1). For this study, we used the GRG catalogue of [Mostert et al. \(2024\)](#) based on LoTSS DR2 ([Shimwell et al. 2019](#)). The catalogue contains 11585 GRGs, the majority of which were identified through an automated, multi-stage pipeline combining machine-learning methods, crowd-sourced classifications, and Bayesian statistical modelling, with the remainder drawn from previously published compilations. This modelling accounts for key selection effects, including surface brightness limitations and identification inefficiencies, thereby enabling constraints on the GRG size distribution, comoving number density, and lobe volume-filling fraction within the cosmic web.

From [Mostert et al. \(2024\)](#) catalogue, we extracted a subset of 285 GRGs located within the SDSS filament catalogue footprint ([Tempel et al. 2014](#)) and have spectroscopic redshifts of  $z \leq 0.155$ . Of these, 221 GRGs were found to lie within a 3D comoving distance of 5 Mpc ( $D_{\text{fil}} \leq 5$  Mpc) from the cosmic filaments (Fig. 1). Given the heterogeneous nature of cosmic filaments, we sought to minimise environmental biases by removing 57 GRGs whose host galaxies are classified as brightest cluster galaxies (BCGs) using WH15 ([Wen & Han 2015](#)). This exclusion ensures that our analysis probes the direct influence of filamentary environments, uncontaminated by the distinct physical conditions of dense cluster cores, and yields a refined working sample of 164 GRGs.

We then performed a detailed morphological classification of each GRG by visually inspecting multi-frequency images from LoTSS DR2 (6'' and 20'' maps at 144 MHz), TGSS ADR1 ( $\sim 25''$  maps at 147 MHz); [Intema et al. 2017](#)), FIRST (5'' maps at 1.4 GHz; [Becker et al. 1995](#)), NVSS (45'' maps at 1.4 GHz; [Condon et al. 1998](#)) and VLASS (2.5'' maps at 3 GHz; [Lacy et al. 2020](#)). LoTSS, with its unparalleled surface-brightness sensitivity, reveals the faint diffuse plasma, while VLASS and FIRST, with their higher angular resolution, resolve compact cores, jets, and terminal hotspots. Together, these complementary datasets allow us to trace compact features, bridge or wing emission, and diffuse relic lobes, thereby establishing a near-complete morphological classification for every source.

We then grouped the sources into the following classes, where  $N$  is the number of sources:

- FRI: centre-brightened jets/plumes ( $N = 29$ )
- FRII: edge-brightened lobes with hotspots ( $N = 56$ )
- WAT: wide-angle tails with C-shaped bends ( $N = 14$ )
- Remnant: lobe-dominated, core-faint systems lacking jets or hotspots ( $N = 18$ )
- Complex: hybrid or ambiguous morphologies that do not fit the above classes ( $N = 19$ )

Morphological classification was not possible for 28 sources due to the lack of publicly available LoTSS data, labelled as "No

data" in the flowchart (Fig. 1). To maintain uniformity and reduce complexity in our subsequent analysis of jet-filament alignment and arm-length ratio, we restrict the study to sources classified as FRII.

## 2.3. The SRG sample

To examine whether SRGs exhibit distinct behaviour compared to GRGs within filament environments, we constructed a comparison sample of SRGs based on the catalogue of [Capetti et al. \(2017\)](#). As with the GRG sample, we restricted the SRGs to those located within the SDSS filament catalogue footprint of [Tempel et al. \(2014\)](#). This SRG catalogue, derived from NVSS, FIRST and SDSS data, contains 122 FRII-type RGs with  $z \leq 0.155$ . We visually inspected all FIRST radio maps to confirm the FRII morphology with compact hotspots and to ensure reliable structural identification. Projected linear sizes were then measured from hotspot to hotspot, as appropriate for FRII morphology. To retain consistency with the SRG definition, one object with a size exceeding 0.7 Mpc was excluded. This process yielded a final set of 102 SRGs.

The 3D comoving distances of these SRGs to the nearest filaments from the [Tempel et al. \(2014\)](#) catalogue were then computed. Of 102 sources, 78 lie within 5 Mpc of filaments ( $D_{\text{fil}} \leq 5$  Mpc; Fig. 2). Cross-matching with the WH15 galaxy cluster catalogue further revealed that 27 of these are hosted by BCGs. Since our aim is to isolate the influence of filaments and avoid biases introduced by dense cluster cores, these BCG-associated SRGs were excluded. The final comparison sample, therefore, consists of 51 FRII SRGs residing in filaments, which we use alongside the GRGs to assess environmental trends.

## 2.4. Extent of the filaments

Unlike virialised haloes, filaments are heterogeneous structures that exhibit a wide range of lengths, widths, and densities. Their lack of spherical symmetry, inherent connectivity, and sensitivity to identification methods pose significant challenges in quantifying how the filamentary environment influences galaxy growth and morphology. The geometry and extent of filaments, particularly their width, set the physical scale over which filaments regulate matter flows, pressure gradients, and gas accretion, thereby impacting the alignment and morphological evolution of galaxies. Filament width refers to the characteristic radial extent from the central spine of a filament to the point where the surrounding matter overdensity, traced by dark matter, gas, or galaxies, drops to a threshold, such as the cosmic mean density ([Wang et al. 2024](#)) or twice the local background density ([Bahe & Jablonka 2025](#)).

The core of a filament is usually considered as the high-density region surrounding the filament spine, where the galaxy and matter overdensity is strongly enhanced compared to the cosmic mean. Observational and simulation studies show that this central region typically extends to a characteristic radius of  $\sim 1\text{--}2$  Mpc ([Cautun et al. 2014; Wang et al. 2024](#)).

Several studies estimate filament widths by stacking filaments in simulations and fitting analytic profiles to their radial density distribution. Using N-body and hydrodynamical simulations, [Colberg et al. \(2005\)](#) and [Dolag et al. \(2006\)](#) fitted isothermal or Navarro-Frenk-White (NFW; [Navarro et al. 1997](#)) like cylindrical profiles to 3D dark matter and gas density distributions, corresponding to filament diameters of  $\sim 2\text{--}5$  Mpc. [Cautun et al. \(2014\)](#) used the NEXUS framework and confirmed these

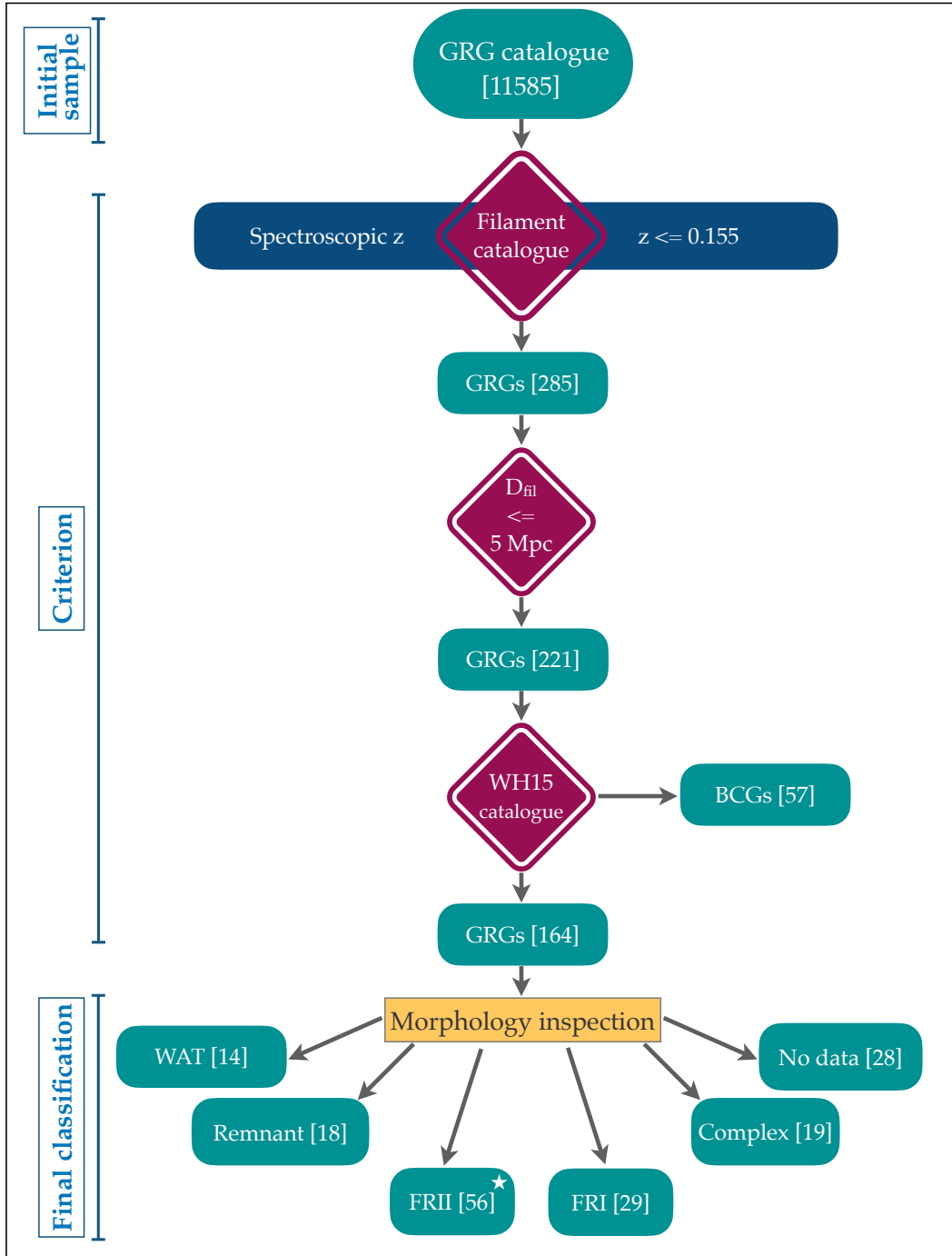


Fig. 1: The flowchart outlines the construction of the GRG sample, combining the [Mostert et al. \(2024\)](#) GRG catalogue with the filament catalogue of [Tempel et al. \(2014\)](#) and excluding the sources found in the WH15 cluster catalogue. The "No data" category denotes sources lacking publicly available LoTSS data, preventing reliable morphological classification.

results across different tracers. [Tanimura et al. \(2020\)](#) analysed stacked thermal Sunyaev-Zel'dovich (tSZ) Compton- $\gamma$  and CMB lensing profiles of filaments identified in the SDSS survey. Their modelling with a  $\beta$ -profile yielded a characteristic full width at half maximum (FWHM) of 2-3 Mpc, providing direct observational evidence for the transverse extent of the dense cores of the cosmic filaments, while the detectable influence of filaments in tSZ and lensing signals extends to about 8 Mpc, reflecting their more diffuse outskirts. [Xia et al. \(2021\)](#), using the Millennium N-body simulation, showed that the tangential velocity of dark mat-

ter around the filaments peaks at radii of the order of 1 to 2 Mpc and declines to negligible levels beyond  $\sim 2$  Mpc, marking the boundary of coherent rotation. Complementing this, [Wang et al. \(2021\)](#) provided observational evidence from SDSS data, detecting a similar rotation curve where galaxy velocities peak around 1 Mpc and fade beyond  $\sim 2$  Mpc. Together, these studies support the interpretation that the core width of cosmic filaments is confined within  $\sim 1$ -2 Mpc. With a different approach, [Wang et al. \(2024\)](#) defined the filament radius as the extent at which the logarithmic slope of the radial density profile reaches a minimum,

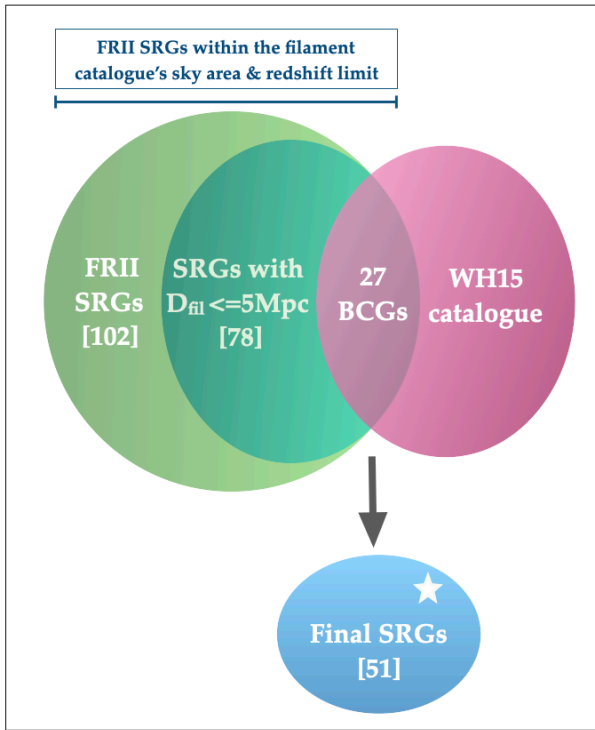


Fig. 2: The figure illustrates the process used to construct the SRG sample used for our analysis.

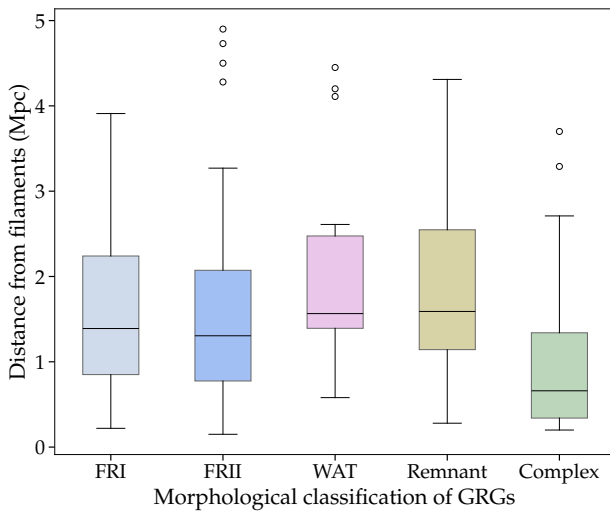


Fig. 3: The box-and-whisker plots present the distributions of distances from filaments for different morphological classes of GRGs: FRI, FRII, WAT, remnant sources, and complex. The black solid line within a box indicates the median of the distribution, the lower and the upper box boundaries represent the 25th percentile (Q1) and 75th percentile (Q3); therefore, the box shows the interquartile (IQR) range of the data. The whiskers denote the range of the distribution within  $1.5 \times \text{IQR}$ , while the circles represent the outliers. As the data are not symmetrically distributed, the whiskers are of unequal length, reflecting the variability above and below the median value. The asymmetry, therefore, indicates skewness or unequal variability in two directions.

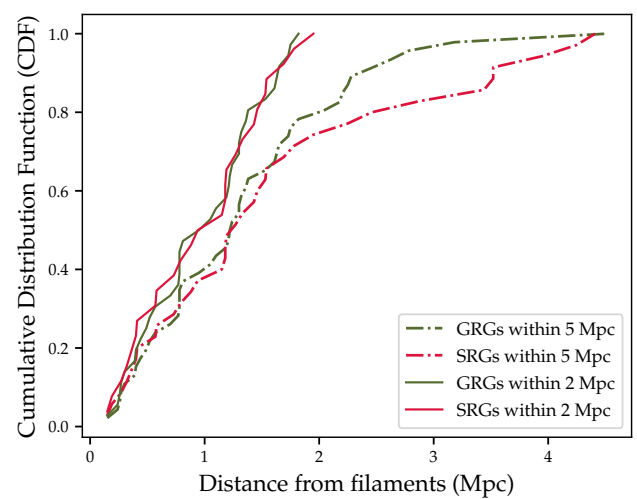


Fig. 4: The plot shows cumulative distribution functions (CDFs) of the 3D distances to the nearest filament spine for GRGs (green) and SRGs (red). For each population, the solid curves correspond to sources within 2 Mpc of the spine and the dashed curves to sources within 5 Mpc.

analogous to the splash-back radius in haloes. They constructed stacked galaxy number density profiles around filament spines in cosmological simulations, which yielded a boundary at  $\sim 0.9$ - $1.3$  Mpc, demarcating the transition between the filament spine and its quasi-linear outskirts. This method captures a physically meaningful edge of the gravitational influence of cosmic filaments.

The study by [Chen et al. \(2015\)](#), based on the MassiveBlack-II hydrodynamical cosmological simulation ([Khandai et al. 2015](#)), demonstrates that the alignment of the galaxy major axes with nearby filament orientations remains statistically significant up to a radial distance of approximately 3.5 Mpc. Within this scale, galaxies, particularly the more massive ones, exhibit a clear tendency to align their major axes along the filament direction, while the alignment signal weakens at larger distances. These findings provide strong evidence that the gravitational and tidal influence of cosmic filaments extends well beyond their dense cores, coherently shaping galaxy orientations across several Mpc. Observationally, [Jung et al. \(2025\)](#) combined LoTSS DR2 with SDSS and Dark Energy Spectroscopic Instrument (DESI) Legacy Imaging Surveys ([Dey et al. 2019](#)) data, showing that massive galaxies within  $\sim 11$  Mpc of filaments align their optical major axes with filament orientations. In contrast, AGN jets, which are typically orthogonal to host galaxy major axes, become more randomly oriented within  $\sim 8$  Mpc of filaments, consistent with chaotic gas accretion and turbulence disrupting stable jet launching.

These studies confirm that, while the dense core of a cosmic filament typically spans  $\sim 1$ - $2$  Mpc, its gravitational tidal field and associated dynamical effects propagate to much larger distances. Signatures such as coherent galaxy spin alignments and anisotropic gas accretion remain detectable several megaparsecs from the filament spine, extending the filament's influence to  $\sim 5$ - $8$  Mpc. Therefore, in our analysis, we consider GRGs and SRGs within 2 Mpc and 5 Mpc of the filament spine to investigate how the cosmic filament environment impacts their growth and morphology.

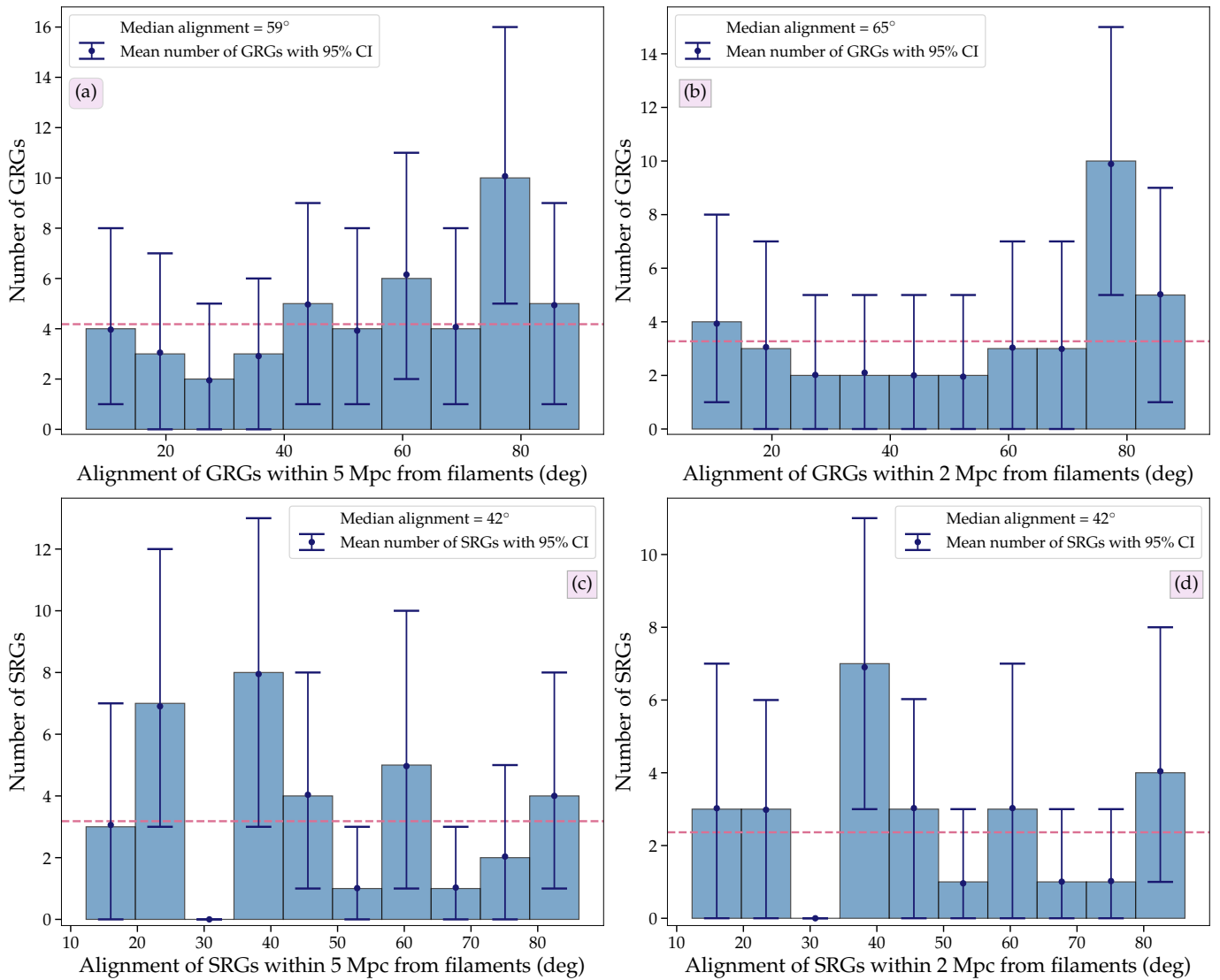


Fig. 5: The figure shows the distribution of jet-filament alignment angles between the radio jet axis and the local filament spine ( $0^\circ$  = parallel,  $90^\circ$  = perpendicular). Panels (a) and (b) present GRGs within 5 Mpc and 2 Mpc of filaments, with median alignments of  $59^\circ$  and  $65^\circ$ , respectively. Panels (c) and (d) show the corresponding SRG distributions, both with a median of  $42^\circ$ . The red dashed line shows the distribution for the uniformly oriented samples. The error bars denote 95% bootstrap (1000 samples) confidence intervals for the mean (blue circles) occupancy of the sources in each bin.

### 3. Analysis of radio galaxies in cosmic filaments

This section outlines the methodology employed for analysing the properties of GRG and SRG samples in cosmic web filaments.

#### 3.1. Distance from the filaments

The distance of a galaxy from the nearest filament serves as a useful statistical proxy, enabling a meaningful investigation into the role of filaments in driving galaxy evolution across the cosmic web. In the [Tempel et al. \(2014\)](#) catalogue, each filament is represented as a spine formed by a sequence of sampling points<sup>2</sup>. For each of these points, the catalogue provides their 3D coordinates: right ascension (RA), declination (Dec) and redshift ( $z$ ).

<sup>2</sup> Defined as the set of points used to probe the galaxy distribution for possible filament presence within the Bisous model framework.

From these data, the Cartesian comoving coordinates ( $x_c, y_c, z_c$ ) of the sampling points that form the filament spines and the host galaxies of the GRGs were derived using the following:

$$x_c = D \sin(90^\circ - \delta) \cos \alpha$$

$$y_c = D \sin(90^\circ - \delta) \sin \alpha$$

$$z_c = D \cos(90^\circ - \delta)$$

where  $\alpha$  = RA,  $\delta$  = Dec, and  $D$  is the comoving distance. Thereafter, the 3D distances between the GRG host galaxy and filament sampling points were calculated, enabling us to identify the filament closest to the GRG host galaxy by finding the closest sampling point of the filament. Using this approach, we identified the filaments closest to the GRG host galaxies and analysed the distribution of the distances of GRGs from their nearest filaments. A box-and-whisker summary of the 3D distances of different classes of GRGs within 5 Mpc from the nearest filament spine is shown in Fig. 3.

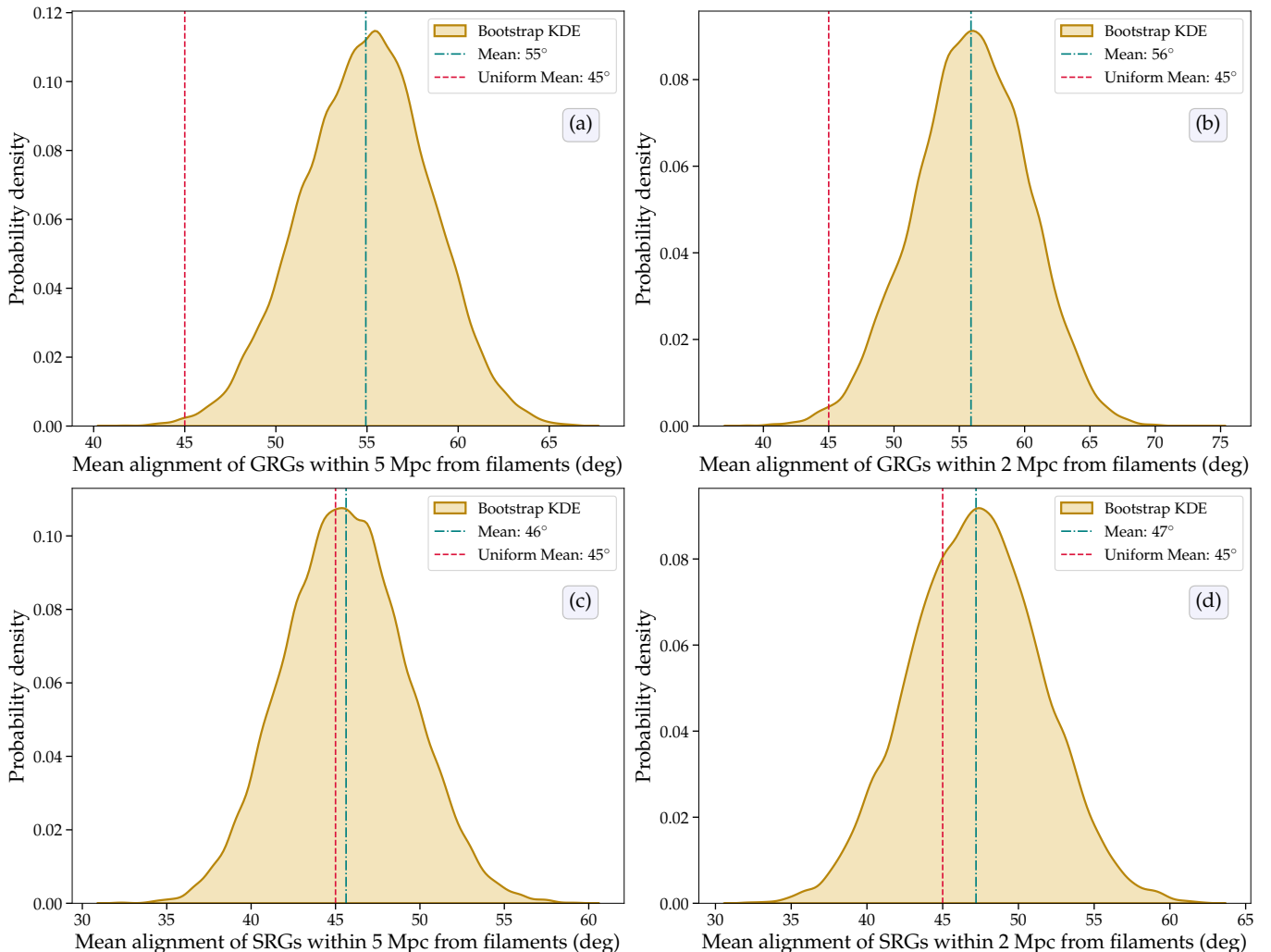


Fig. 6: The plot shows the kernel density estimations (KDEs) of mean jet-filaments alignments in 1000 bootstrap realisations. Panels (a), (b), (c) and (d) represent the estimates for GRGs within 5 Mpc, GRGs within 2 Mpc, SRGs within 5 Mpc and SRGs within 2 Mpc of filaments. The red dashed vertical line marks the uniform mean, and the green dashed vertical line marks the bootstrap mean from 1000 resamples for the corresponding subsets.

For comparison, we also analysed a control sample of SRGs, applying the same methodology to determine their 3D distances from the nearest cosmic filaments. Sources, for which the nearest filament point corresponded to the filament end-point, were excluded from both samples as filament terminations are not well-defined and may introduce ambiguity in assessing the influence of the filamentary environment. In this analysis, we considered FRII GRGs and FRII SRGs located within 5 Mpc (GRGs: 46, SRGs: 35) and 2 Mpc (GRGs: 36, SRGs: 26) of filament spine (see Tab. B.1 in Appendix B). The resulting distance distributions are shown in Fig. 4.

### 3.2. Orientation with respect to filaments

Given the complexity of AGN activity, analysing jet alignments with cosmic filaments in a statistical framework offers a robust means of identifying underlying trends. Such analyses are essential for understanding how anisotropic filamentary environments influence the structural and dynamical evolution of radio AGN.

Since the filaments are inherently curvilinear structures, the filament axis for determining the alignment of radio jets, particu-

larly in FRII GRGs and SRGs, is defined as the projected straight line (on the sky plane) connecting the two sampling points adjacent to the nearest filament sampling point (Sec. 3.1). Sources for which the nearest filament point lies at the filament terminus were excluded from the alignment analysis, as filament ends are not well defined.

For simplicity, the axis of each GRG (and SRG) is defined as the line segment connecting its two radio hotspots on the sky plane. Therefore, accurately identifying the exact locations of the hotspots is essential for a reliable axis determination. To achieve this, we visually inspected the multi-frequency radio images from multiple radio surveys (see Sec. 2.2). The hotspot coordinates (RA, Dec) were taken from the highest-frequency maps available, provided that the compact hotspot emission was detected at a significance level of at least  $3\sigma$  above the rms noise. This has been illustrated in the figures in Sec. A.

The position angles of the GRGs were derived from the coordinates of their radio hotspots, while the position angles of the filaments were calculated from the 2D (RA, Dec) locations of the filament sampling points that define the local filament axis, as described above. The minimum angle between each GRG axis

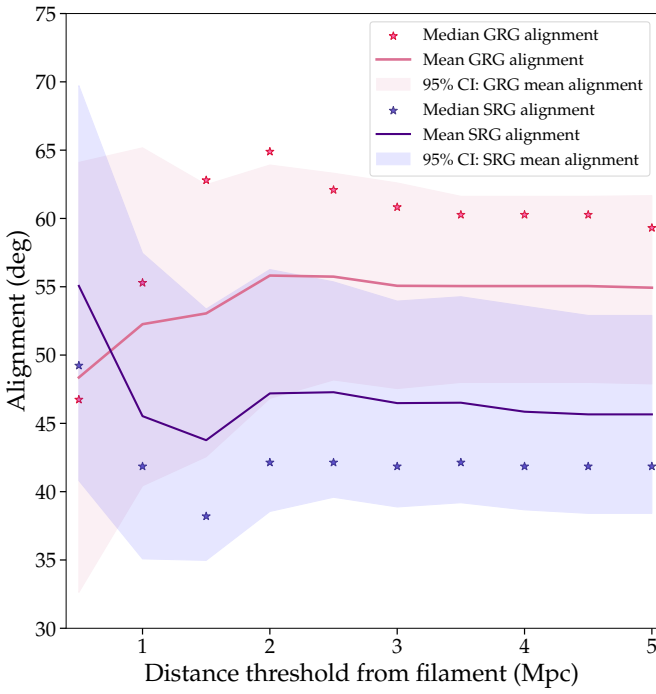


Fig. 7: The plot shows how GRG and SRG mean jet-alignments change with distance threshold from filaments. The solid red curve traces the GRG mean, the pink shaded region denotes the 95% bootstrap CI, and red stars mark the median alignment in each distance bin. The solid blue curve represents the SRG mean, the lavender band shows the 95% bootstrap CI, and blue stars mark the corresponding medians.

and its nearest filament was then obtained by taking the absolute difference between these position angles (for radio jet axis position angle uncertainties see Appendix. C). This angle served

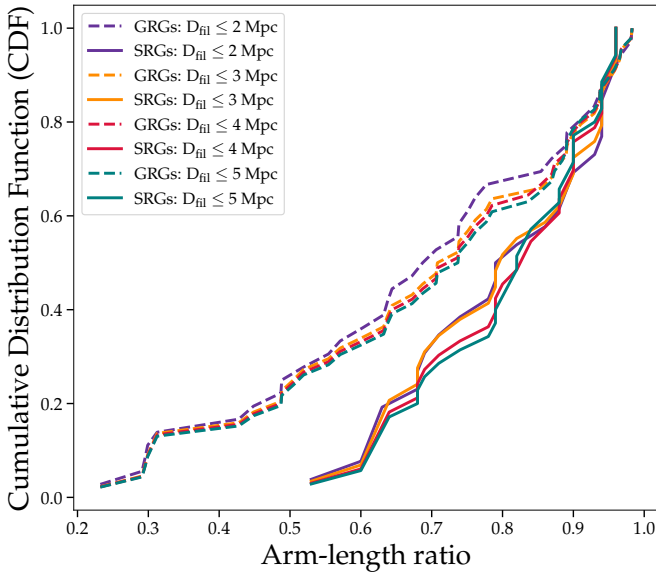


Fig. 8: The figure displays the cumulative arm-length ratio (ALR) distributions for GRGs (dashed curve), and SRGs (solid curve), stratified by proximity to the nearest filament spine: 2 Mpc (blue), 3 Mpc (orange), 4 Mpc (red), and 5 Mpc (green).

as a quantitative measure of the alignment between the radio jet and the filament axis. The same methodology was employed to assess the alignment of SRGs with the filament axis.

As the original sample sizes for both GRGs and SRGs are relatively small, we generated 1000 bootstrap samples for each population to construct empirical sampling distributions, thereby capturing the inherent variability in the data and providing a robust basis for estimating confidence intervals and assessing potential trends. Each bootstrap realisation was constructed by drawing, with replacement, the same number of objects as in the observed sample; we then repeated the identical analysis on every realisation. For each bootstrap realisation, we computed the number of objects in each bin, yielding a distribution of source counts per bin across the 1000 realisations. From these distributions, we obtained, for each bin, the mean bootstrap count and the corresponding 95% confidence interval. The resulting error bars are generally asymmetric, reflecting the asymmetry of the underlying bootstrap distributions of source counts per bin (Fig. 5).

### 3.3. Arm-length ratio

In the simplest scenario, radio galaxies launch bipolar relativistic jets in opposite directions, each transporting comparable amounts of energy, and in principle, producing symmetric radio structures. In practice, however, this symmetry is frequently disrupted by environmental influences. If the jet, or its associated lobe, encounters a denser region of the IGM, it undergoes stronger interactions with the surrounding material, which in turn impedes its propagation. The increased resistance reduces the projected distance that the jet can advance from the radio core, giving rise to a shorter arm. The resulting morphology is thus asymmetric, with one lobe extending farther than the other. Such asymmetry provides a valuable diagnostic for probing the influence of the environment on the properties and evolution of RGs. A widely used parameter to quantify this effect is the arm-length ratio (ALR), defined as the ratio of the projected length of the shorter arm to that of the longer arm.

In our study, we examined the ALRs of FRII-type GRGs and SRGs, excluding sources located near the terminal regions of filaments, to assess the influence of cosmic web filaments on their growth and morphological development. The projected arm lengths were derived from the angular separations of the radio hotspots with respect to the host galaxy. By definition, the arm with the smaller angular separation was taken as the shorter arm, while the larger separation defined the longer arm. The ratio of these two values yields the ALR, which serves as a quantitative measure of morphological asymmetry and enables a direct comparison between GRGs and SRGs.

## 4. Results

### 4.1. Distance from the filaments

The box-and-whisker plot in Fig. 3 depicts the distribution of comoving 3D distances from filaments for different morphological classes – FRI, FRII, WAT, remnant, and complex among 136 GRGs located within 5 Mpc of filaments. GRGs with complex morphology exhibit the smallest median distance from filaments (0.66 Mpc), indicating a pronounced tendency for such sources to be located in close proximity to filamentary structures. Such locations, typically associated with enhanced galaxy and gas densities, may facilitate interactions or mergers that could contribute to the development of complex radio structures. In

comparison, FRI and FRII sources exhibit median distances of 1.39 Mpc and 1.31 Mpc, respectively; their comparable values suggest similar environmental conditions influencing their growth. WAT and remnant sources lie slightly farther from filaments, with median distances of 1.56 Mpc and 1.59 Mpc, respectively, indicating that these classes may preferentially occur in regions less tightly associated with filamentary spines compared to other morphological types. This environmental preference may reflect different evolutionary stages, with WATs potentially tracing dynamically active group or cluster outskirts (O’Dea & Baum 2023), and remnants representing fading RGs (Morganti 2024) that have migrated or evolved away from the densest filamentary environments. These systematic differences in median distances across morphological classes highlight the potential role of cosmic web environments in shaping the morphological diversity of GRGs, possibly through a combination of environmental fuelling, dynamical interactions, and evolutionary ageing.

Fig. 4 shows the cumulative distribution functions of distances from cosmic filaments for FRII SRGs and GRGs, considering only sources whose host galaxies are within 2 and 5 Mpc of the filament spines, and excluding sources located at filament ends. For sources within 2 Mpc of filaments, the median distances are 1.04 Mpc for SRGs and 1.00 Mpc for GRGs; for those within 5 Mpc, the corresponding values are 1.27 Mpc and 1.23 Mpc, respectively. The close agreement between these values, together with the substantial overlap in their cumulative distributions, indicates that SRGs and GRGs exhibit comparable levels of occupancy within the filament environment. This uniformity in large-scale spatial association suggests that proximity to filaments alone is insufficient to account for the size difference between the two populations. Additional factors, such as jet-filament alignment and intrinsic host galaxy properties, are likely to play a more decisive role in determining whether a radio galaxy evolves into a giant.

Additionally, to examine whether the projected linear sizes of RGs depend on their proximity to filaments, we tested for correlations between source size and distance to the filament spine. No statistically significant relationship was found for either the SRG or GRG populations. Both populations, however, show a mild excess of sources near filament axes, possibly reflecting enhanced fuelling within filament cores that promotes the growth of RGs.

#### 4.2. Orientation with respect to filaments

The distribution of orientation angles of GRGs, along with their 1000 bootstrap realisations, located within 5 Mpc of filaments is shown in Fig. 5a. The median orientation angle of the observational GRG sample ( $59^\circ$ ) is in close agreement with that of the corresponding bootstrap median ( $60^\circ$ ), indicating a stable alignment at this scale. When the analysis is restricted to GRGs within 2 Mpc of filaments (Fig. 5b), the bootstrap median increases slightly to  $65^\circ$ , remaining consistent with the median value of the observational sample. This similarity across distance thresholds suggests that the observed alignment is robust to variations in the proximity criterion to the filaments. In both figures, the error bars represent the 95% confidence interval around the mean number of GRGs per orientation bin, while the red dotted line indicates the expected distribution for a uniform orientation. In both cases, the distributions confirm a tendency for GRGs to be preferentially aligned at larger angles relative to the filament spine.

Fig. 5c,d show the orientation distributions of SRGs within 5 and 2 Mpc of filaments, together with 1000 bootstrap samples. In both cases, the median angle is  $42^\circ$ , identical to the bootstrap median and statistically indistinguishable from the random expectation of  $45^\circ$  given the 95% confidence intervals. Error bars denote the 95% confidence intervals around the mean counts per bin, and the red dotted line marks the uniform distribution. These results indicate no significant preferential alignment for SRGs, whose orientations remain consistent across distance thresholds. By contrast, GRGs exhibit median offsets by  $\sim 15^\circ$  from the random expectation, a deviation significant beyond the 95% level and consistent with their corresponding mean offsets. The two populations, therefore, show a clear dichotomy: SRGs are consistent with random orientations, while GRGs preferentially align at larger angles to filament spines.

To assess the robustness of the alignment trends, we constructed kernel density estimates (KDEs) of the mean orientations obtained from each bootstrap realisation for both GRGs and SRGs, considering sources located within 5 Mpc and 2 Mpc of the filament spine. For GRGs within 5 Mpc (Fig. 6a), the bootstrap distribution peaks at a mean orientation of  $\sim 55^\circ$  (green dotted line), which lies well above  $45^\circ$ , shown by red dotted line – the expectation for a uniform orientation distribution. This offset corresponds to a deviation of  $\sim 2.9\sigma$  ( $p \approx 0.0042$ ), with 99.8% of the bootstrap means exceeding  $45^\circ$  indicating a statistically significant departure from uniformity. A consistent trend is observed for GRGs within 2 Mpc (Fig. 6b), where the mean orientation is  $\sim 56^\circ$  with 99.6% of bootstrap means lying above  $45^\circ$ , and the deviation from uniformity remains highly significant. These results confirm that the preferential alignment of GRGs at larger angles relative to the filament spine is stable across distance thresholds. In contrast, SRGs exhibit no such preference. The KDEs of the mean orientations of bootstrapped SRG samples within 5 Mpc (Fig. 6c) and 2 Mpc (Fig. 6d) peak at  $\sim 46^\circ$  and  $\sim 47^\circ$ , respectively. The proportions of bootstrap means above  $45^\circ$  are  $\sim 56\%$  and  $\sim 68\%$ , which are consistent with sampling variability under a uniform distribution. The deviations from uniformity are only  $\sim 0.18\sigma$  ( $p \approx 0.44$ ), which are statistically insignificant, indicating that SRG jet orientations are consistent with randomness relative to the filament axis.

We further examined the mean and median orientations of both GRGs and SRGs as a function of distance from filaments, varying the threshold from 5 Mpc to 0.5 Mpc (Fig. 7). For thresholds between 2 Mpc and 5 Mpc, GRGs consistently display mean and median orientations significantly above the uniform expectation, while SRGs remain consistent with random alignment within 95% confidence intervals. Below 2 Mpc, the reduced sample sizes limit any statistically significant inferences.

To quantitatively test the null hypothesis of uniformity, we applied both the Kolmogorov–Smirnov (KS) and Anderson–Darling (AD) tests across the range of distance thresholds. For GRGs, KS test  $p$ -values satisfy  $p \leq 0.02$  and AD test  $p \leq 0.01$ , providing strong evidence against uniformity. For SRGs, the KS test yields  $p \geq 0.4$  and the AD test  $p \geq 0.3$ , indicating no significant departure from random orientation.

Overall, the bootstrap analyses, distance-dependent trends, and statistical tests consistently reveal a clear dichotomy between the two populations: GRGs show a significant tendency to orient at larger angles relative to the filament spine, whereas SRGs are consistent with random orientation. This contrast likely reflects intrinsic differences in how the two classes interact with the filamentary environment and in their subsequent evolutionary pathways.

Our jet-filament angles are measured in projection on the plane of the sky. For radio galaxies, especially the extended FRII systems that dominate the GRG class, AGN unification (e.g., [Urry & Padovani 1995](#)), their low core dominance and well-resolved, bipolar edge-brightened morphologies imply viewing angles close to the sky plane. For such sources, the projected radio axis closely traces the intrinsic jet direction, and hence the projection effect on the jet position angle is minimal. Moreover, the projection of the filament spine removes only the line-of-sight component and therefore tends to move intrinsically extreme alignments towards more moderate apparent angles. Consequently, the large alignment angles we report are conservative lower limits to the actual alignments. We performed bootstrap resampling of the alignment measurements, which yields stable and consistent angle distributions, supporting the robustness of our results.

#### 4.3. Arm-length ratio

Symmetry in RGs is often disrupted by their surrounding environment, making ALR a useful probe of how external conditions influence source morphology. In this section, we examine how ALR varies with filamentary environment, testing whether asymmetries correlate with distance to filament spines. For example, [Pirya et al. \(2012\)](#) reported that in 3C 326 the pronounced arm length asymmetry is linked to a nearby filamentary overdensity, and suggested that similar environmental anisotropies may underlie lobe asymmetries in other RGs.

Fig. 8 shows the cumulative distribution functions of ALR for SRGs and GRGs based on their proximity to the filaments. The distribution highlights systematic differences in asymmetry between the two populations across different distance thresholds. For GRGs, the mean and median ALR within 5 Mpc of filaments are 0.69 and 0.73, respectively, decreasing slightly to 0.67 and 0.69 within 2 Mpc. By contrast, SRGs display higher and more consistent values, with a mean and median of 0.81 and 0.82 within 5 Mpc, and 0.80 and 0.80 within 2 Mpc of filaments. The lower ALR values in GRGs, especially in proximity to filaments, indicate a greater degree of structural asymmetry relative to SRGs. This trend suggests that the larger physical extents of GRGs render them more susceptible to anisotropies in the ambient medium, amplifying the influence of the filamentary environment on their jet propagation and overall morphology. In contrast, the relative stability of ALR in SRGs across filament distances implies a weaker environmental impact.

## 5. Discussion: Environmental coupling of radio galaxies within cosmic filaments

Cosmic web filaments, the principal components of the large-scale structure, trace the distribution of dark and baryonic matter and serve as conduits for gas flows, galaxy evolution, and matter transport. They form a dynamic environment in which galaxies and their radio jets interact with anisotropic gas streams, pressure gradients, and magnetic fields ([Bond et al. 1996](#); [Dubois et al. 2014](#); [Cautun et al. 2014](#); [Wang et al. 2024](#)). Striking individual systems already demonstrate how profoundly filaments and sheets can reshape radio galaxy morphology. The GRG 0503–286, for example, displays a remarkable inversion-symmetric, X-shaped structure, with its lobes sharply bent away from the source axis and separated by a  $\sim 200$  kpc emission-free gap ([Dabhade & Krishna 2022](#)). This unusual morphology cannot be explained by host-centred processes alone; in-

stead, it is best interpreted as the deflection of lobe backflows by a large-scale sheet of the cosmic web, consistent with density asymmetries and Warm Hot Intergalactic Medium (WHIM)-like gas acting across megaparsec scales. Such cases illustrate the rich astrophysics that can be extracted from radio galaxies as probes of the intergalactic medium, revealing the role of sheet- and filament-driven anisotropic pressure, buoyancy, and large-scale tidal fields. Yet, before these environmental imprints can be interpreted at a population level, the essential first step is to robustly identify RGs within filaments and to locate them precisely with respect to the filament spine and boundaries. In this work, we address this gap by identifying RGs within a three-dimensional filamentary framework and systematically examining their properties across distinct filament environments. By doing so, we provide a framework enabling a quantitative assessment of how the cosmic web filament influences their growth, asymmetries, and feedback.

#### 5.1. Proximity to filament: impact on morphology

The analysis of filament environments across different GRG morphological classes reveals that complex sources ( $\sim 18\%$  of the sample) exhibit a pronounced preference for close proximity to filament spines, exhibiting a median distance of 0.66 Mpc (Fig. 3). At such small separations, the host galaxies reside in regions of elevated matter density and coherent flows characteristic of filament cores. These environments are subject to enhanced gravitational interactions and tidal forces, which can induce asymmetries in the accretion flow, perturb the stability of the radio jets, and distort their propagation paths. Such conditions hinder the development of the symmetric, well-collimated lobes characteristic of classical FR morphologies, instead producing irregular or disrupted radio structures that manifest observationally as complex morphologies. This suggests that the complex class may, at least in part, represent GRGs whose evolutionary trajectory has been shaped by strong environmental modulation within the densest regions of the cosmic web.

The overall filament occupancy of GRGs is not significantly different from that of SRGs (Fig. 4), indicating that large-scale filament proximity alone does not govern the transition from smaller to giant radio galaxies. Instead, the eventual size and morphology are more likely determined by the interplay of multiple factors, including jet-filament alignment, variations in local galaxy density, episodic AGN activity, and the intrinsic physical properties of the host galaxy.

#### 5.2. GRG-filament alignment: impact on GRG growth

Within cosmic web filaments, matter tends to flow along the filament's spine towards denser nodes, such as galaxy clusters and superclusters, where gravitational potential wells are the deepest. Perpendicular to the spine, material from surrounding voids accretes into the filament's high-density axis. These large-scale gravitational flows generate anisotropies in the gas density and pressure around galaxies ([Gheller & Vazza 2019](#)), which can influence AGN fueling by providing a preferred direction for gas inflow, and can also impact jet propagation by creating directional variations in the ambient medium. For RGs residing in such environments, the orientation of the radio axis relative to the filament spine becomes very important for their growth. Jets aligned parallel to the filament may encounter systematically denser, more turbulent media shaped by longitudinal flows toward nodes, whereas jets directed perpendicular to the spine

may propagate into comparatively diffuse void-bound regions. Fig. A.1, Fig. A.2 and Fig. A.3 in Appendix A are the examples of GRGs aligning nearly parallel, almost perpendicular and at an intermediate angle of 29° with their local filament axes. Over the long lifetimes required for GRGs to reach megaparsec scales, these directional differences in the external medium can imprint themselves on source morphology, affecting jet bending, orientation of jet axes, and potentially contributing to variations in ALRs.

Based on our findings, GRGs tend to exhibit preferentially large angles between their radio jet axes and the filament spine, in contrast to SRGs, which show random orientations. This distinction suggests varied environmental coupling at different physical scales and evolutionary stages of RGs. A GRG oriented at a large angle to the filament spine will likely have one or both jets propagating almost perpendicular to the spine into lower-density, void-facing regions rather than along the denser filament axis as seen in objects studied by Malarecki et al. (2015) and Oei et al. (2024). Such conditions would reduce resistance to jet advancement, enabling the lobes to expand farther before significant dissipation, thereby facilitating the extreme linear sizes of GRGs. This geometry can facilitate steady lobe advancement over tens to hundreds of millions of years (Myr) required to reach Mpc scales (e.g., Jamrozy et al. 2008; Dabhade et al. 2023). Such sustained growth also implies a stable jet orientation, which in turn points to prolonged, coherent accretion onto the central engine, the conditions consistent with quasi-steady fuelling modes that preserve jet directionality (e.g., Liska et al. 2019). Altogether, these results suggest a pathway to the giant regime: RGs with sustained fuelling and jets oriented far from the filament axis are the systems most likely to evolve into GRGs.

### 5.3. Environmental gradients: asymmetry in GRGs

Using our SRG and GRG samples, we tested for statistical trends between jet-filament alignment, ALR and proximity to filament axis, if any, and found no statistically significant correlations in either population. This suggests that the observed lobe asymmetry primarily arises from local conditions such as density variations, small-scale IGM inhomogeneities, and turbulence. Nonetheless, we observe a systematic offset in ALR, with GRGs being more asymmetric on average than SRGs. This is consistent with the fact that GRG lobes traverse longer path lengths through a more anisotropic medium, integrating modest environmental contrasts into appreciable length asymmetries. Consistent with the orientation results, GRGs aligned at large angles to filament spines are likely to encounter steeper transverse density gradients from the spine toward the void-facing regions. Such gradients modulate the advance speeds of the two hotspots differently, enhancing asymmetry in GRGs relative to SRGs, whose jets likely evolve in a more uniform environment with milder pressure differences.

These interpretations are further supported by our ALR statistics. In a filamentary environment, anisotropic density and pressure fields, in general, imply that an RG oriented at a large angle to the filament spine will tend to drive its outward lobe into the lower-density inter-filament medium, favouring faster advancement, while its inward lobe encounters the denser spine, resulting in slower advancement and confinement (as seen in asymmetric GRGs shown in Fig. A.1 and Fig. A.2). Consistent with this expectation, our GRG sample, already more asymmetric than SRGs, shows 54% of sources with the shorter arm towards the spine and 46% with the shorter arm towards the

periphery. Sources (e.g., 54% GRGs) with spine-facing shorter arms experience higher effective ram pressure along their path. Sources (e.g., 46% GRGs) with a shorter peripheral arm could possibly be explained by local inhomogeneities along the outward path or by interaction with void-to-spine transverse inflow acting as an opposing bulk flow, both consistent with the inhomogeneous nature of filaments. For SRGs, 63% have the shorter arm away from the spine and 37% towards the spine. Given their random jet-spine orientations and smaller sizes, the SRG statistics point to local environmental interactions as the primary driver of asymmetry. The absence of pronounced asymmetry in SRGs suggests that filament-driven effects become significant only once jets and lobes extend to Mpc scales; SRGs remain too small to sample these large-scale gradients.

## 6. Summary and future prospects

Our analysis focuses on GRGs, selected from Mostert et al. (2024) that lie within cosmic-web filaments traced on the SDSS footprint by Tempel et al. (2014), and compares them with a control sample of SRGs from Capetti et al. (2017) restricted to the same sky area and environmental selection. After applying the selection criteria (see Fig. 1), the final sample comprises 164 GRGs, including 56 of FRII type. Similarly, the Capetti et al. (2017) catalogue provided 51 FRII SRGs used in the analysis.

The results of our study are summarised as follows:

- For both GRGs and SRGs, no statistically significant correlation is found between projected size and 3D comoving distance to the nearest filament spine. However, both populations show a spatial excess within  $\sim 2$  Mpc of the spine, implying that the enhanced gas supply in filament cores supports the development of extended radio structures.
- We find a clear morphological segregation with filament proximity: complex sources occur nearest to the spine, classical FRI/FRII systems at intermediate distances, and WATs and remnants farther out. The denser, more turbulent filament spine region likely promotes anisotropic ram pressure and jet interactions, giving rise to complex structures. At intermediate distances, smoother conditions favour stable jet collimation in FRIIs and gradual deceleration in FRIIs. In the outskirts, weaker confinement and crosswinds allow WATs to flare, while the low external pressure enables remnant lobes to expand and persist after jet switch-off.
- FRII GRGs exhibit larger alignment angles between their radio jet axes and the filament spine, whereas FRII SRGs display a random orientation distribution. This supports a scenario in which GRG jets preferentially propagate into lower-resistance, void-facing regions, reducing effective ram pressure and facilitating larger growth.
- FRII GRGs (lower ALR) are more asymmetric than FRII SRGs, consistent with steeper transverse spine-to-void environmental gradients that differentially modulate hotspots' advance speeds toward and away from the spine, and enhance lobe-length disparities.
- The ALR trends are consistent with the orientation results, indicating that GRGs positioned nearly perpendicular to filament spines experience stronger transverse density gradients, leading to greater lobe asymmetries driven by unequal hotspot advancement.

Our results demonstrate that connecting radio galaxy morphology to the structure of the cosmic web is now within observational reach. By accurately locating GRGs and SRGs within

filaments, we establish a framework for probing how the thermodynamic and magnetic properties of large-scale environments shape AGN evolution. This opens the way for a new generation of studies that will move beyond statistical correlations to direct measurements of the intergalactic medium within filaments. Upcoming facilities such as the Square Kilometre Array (SKA<sup>3</sup>; [Braun et al. 2019](#)), LOFAR-2.0<sup>4</sup>, and the 4-metre Multi-Object Spectroscopic Telescope (4MOST; [de Jong et al. 2019](#)), combined with deep X-ray and optical surveys, will enable high-resolution polarimetric and spectral diagnostics capable of tracing pressure, magnetic fields, and feedback processes across the cosmic web. Together, these efforts promise to transform radio galaxies into precision tools for mapping the physical state and evolution of the filamentary Universe.

**Acknowledgements.** This work was supported by the Estonian Ministry of Education and Research (grant TK202), Estonian Research Council grants (PRG1006, PRG3034, PSG1045) and the European Union’s Horizon Europe research and innovation programme (EXCOSM, grant No. 101159513). We acknowledge that this work has made use of ASTROPY ([Astropy Collaboration et al. 2013](#)), APLPY ([Robitaille & Bressert 2012](#)), MATPLOTLIB ([Hunter 2007](#)), TOPCAT ([Taylor 2005](#)) and the legacy surveys <https://www.legacysurvey.org/acknowledgment/>.

## References

Aihara, H., Allende Prieto, C., An, D., et al. 2011, *ApJS*, 193, 29

Astropy Collaboration, Robitaille, T. P., Tollerud, E. J., et al. 2013, *A&A*, 558, A33

Bahe, Y. M. & Jablonka, P. 2025, arXiv e-prints, arXiv:2502.06484

Becker, R. H., White, R. L., & Helfand, D. J. 1995, *ApJ*, 450, 559

Blandford, R., Meier, D., & Readhead, A. 2019, *ARA&A*, 57, 467

Bond, J. R., Kofman, L., & Pogosyan, D. 1996, *Nature*, 380, 603

Braun, R., Bonaldi, A., Bourke, T., Keane, E., & Wagg, J. 2019, arXiv e-prints, arXiv:1912.12699

Capetti, A., Massaro, F., & Baldi, R. D. 2017, *A&A*, 601, A81

Casadei, S., Capetti, A., Raiteri, C. M., & Massaro, F. 2024, *A&A*, 684, A159

Cautun, M., van de Weygaert, R., Jones, B. J. T., & Frenk, C. S. 2014, *MNRAS*, 441, 2923

Chen, Y.-C., Ho, S., Tenneti, A., et al. 2015, *MNRAS*, 454, 3341

Colberg, J. M., Krughoff, K. S., & Connolly, A. J. 2005, *MNRAS*, 359, 272

Condon, J. J. 1997, *PASP*, 109, 166

Condon, J. J., Cotton, W. D., Greisen, E. W., et al. 1998, *AJ*, 115, 1693

Dabhadse, P., Chavan, K., Saikia, D. J., Oei, M. S. S. L., & Röttgering, H. J. A. 2025, *A&A*, 696, A97

Dabhadse, P. & Krishna, G. 2022, *A&A*, 660, L10

Dabhadse, P., Mahato, M., Bagchi, J., et al. 2020a, *A&A*, 642, A153

Dabhadse, P., Röttgering, H. J. A., Bagchi, J., et al. 2020b, *A&A*, 635, A5

Dabhadse, P., Saikia, D. J., & Mahato, M. 2023, *Journal of Astrophysics and Astronomy*, 44, 13

de Jong, R. S., Agertz, O., Berbel, A. A., et al. 2019, *The Messenger*, 175, 3

Dey, A., Schlegel, D. J., Lang, D., et al. 2019, *AJ*, 157, 168

Dolag, K., Meneghetti, M., Moscardini, L., Rasia, E., & Bonaldi, A. 2006, *MNRAS*, 370, 656

Dubois, Y., Pichon, C., Welker, C., et al. 2014, *MNRAS*, 444, 1453

Fanaroff, B. L. & Riley, J. M. 1974, *MNRAS*, 167, 31P

Fomalont, E. B. 1999, in *Astronomical Society of the Pacific Conference Series*, Vol. 180, *Synthesis Imaging in Radio Astronomy II*, ed. G. B. Taylor, C. L. Carilli, & R. A. Perley, 301

Gheller, C. & Vazza, F. 2019, *MNRAS*, 486, 981

Gopal-Krishna, Wiita, P. J., & Saripalli, L. 1989, *MNRAS*, 239, 173

Hunter, J. D. 2007, *Computing in Science and Engineering*, 9, 90

Intema, H. T., Jagannathan, P., Mooley, K. P., & Frail, D. A. 2017, *A&A*, 598, A78

Jamrozy, M., Konar, C., Machalski, J., & Saikia, D. J. 2008, *MNRAS*, 385, 1286

Jung, S. L., Whittam, I. H., Jarvis, M. J., et al. 2025, *MNRAS*, 539, 2362

Khandai, N., Di Matteo, T., Croft, R., et al. 2015, *MNRAS*, 450, 1349

Lacy, M., Baum, S. A., Chandler, C. J., et al. 2020, *PASP*, 132, 035001

Lan, T.-W. & Prochaska, J. X. 2021, *MNRAS*, 502, 5104

Liska, M., Tchekhovskoy, A., Ingram, A., & van der Klis, M. 2019, *MNRAS*, 487, 550

Mack, K. H., Klein, U., O’Dea, C. P., Willis, A. G., & Saripalli, L. 1998, *A&A*, 329, 431

Malarecki, J. M., Jones, D. H., Saripalli, L., Staveley-Smith, L., & Subrahmanyam, R. 2015, *MNRAS*, 449, 955

Massaro, F., Álvarez-Crespo, N., Capetti, A., et al. 2019, *ApJS*, 240, 20

Morganti, R. 2024, *Galaxies*, 12, 11

Mostert, R. I. J., Oei, M. S. S. L., Barkus, B., et al. 2024, *A&A*, 691, A185

Navarro, J. F., Frenk, C. S., & White, S. D. M. 1997, *ApJ*, 490, 493

O’Dea, C. P. & Baum, S. A. 2023, *Galaxies*, 11, 67

Oei, M. S. S. L., Hardcastle, M. J., Timmerman, R., et al. 2024, *Nature*, 633, 537

Oei, M. S. S. L., van Weeren, R. J., Hardcastle, M. J., et al. 2022, *A&A*, 660, A2

Oei, M. S. S. L., van Weeren, R. J., Hardcastle, M. J., et al. 2024, *A&A*, 686, A137

Piry, A., Saikia, D. J., Singh, M., & Chandola, H. C. 2012, *MNRAS*, 426, 758

Planck Collaboration, Ade, P. A. R., Aghanim, N., et al. 2016, *A&A*, 594, A13

Robitaille, T. & Bressert, E. 2012, *APLpy: Astronomical Plotting Library in Python*

Sankhayan, S. & Dabhadse, P. 2024, *A&A*, 687, L8

Shimwell, T. W., Tasse, C., Hardcastle, M. J., et al. 2019, *A&A*, 622, A1

Stoica, R. S., Martínez, V. J., Mateu, J., & Saar, E. 2005, *A&A*, 434, 423

Stuardi, C., O’Sullivan, S. P., Bonafede, A., et al. 2020, *A&A*, 638, A48

Tanimura, H., Aghanim, N., Bonjean, V., Malavasi, N., & Douspis, M. 2020, *A&A*, 637, A41

Taylor, M. B. 2005, in *Astronomical Society of the Pacific Conference Series*, Vol. 347, *Astronomical Data Analysis Software and Systems XIV*, ed. P. Shopbell, M. Britton, & R. Ebert, 29

Tempel, E., Stoica, R. S., Kipper, R., & Saar, E. 2016, *Astronomy and Computing*, 16, 17

Tempel, E., Stoica, R. S., Martínez, V. J., et al. 2014, *MNRAS*, 438, 3465

Urry, C. M. & Padovani, P. 1995, *PASP*, 107, 803

Wang, P., Libeskind, N. I., Tempel, E., Kang, X., & Guo, Q. 2021, *Nature Astronomy*, 5, 839

Wang, W., Wang, P., Guo, H., et al. 2024, *MNRAS*, 532, 4604

Wen, Z. L. & Han, J. L. 2015, *ApJ*, 807, 178

Wiita, P. J., Rosen, A., Gopal-Krishna, & Saripalli, L. 1989, *Giant Radio Galaxies via Inverse Compton Weakened Jets*, ed. K. Meisenheimer & H.-J. Roeser, Vol. 327, 173

Willis, A. G., Strom, R. G., & Wilson, A. S. 1974, *Nature*, 250, 625

Xia, Q., Neyrinck, M. C., Cai, Y.-C., & Aragón-Calvo, M. A. 2021, *MNRAS*, 506, 1059

York, D. G., Adelman, J., Anderson, Jr., J. E., et al. 2000, *AJ*, 120, 1579

<sup>3</sup> <https://www.skao.int/en>

<sup>4</sup> <https://www.lofar.eu/lofar2-0-documentation/>

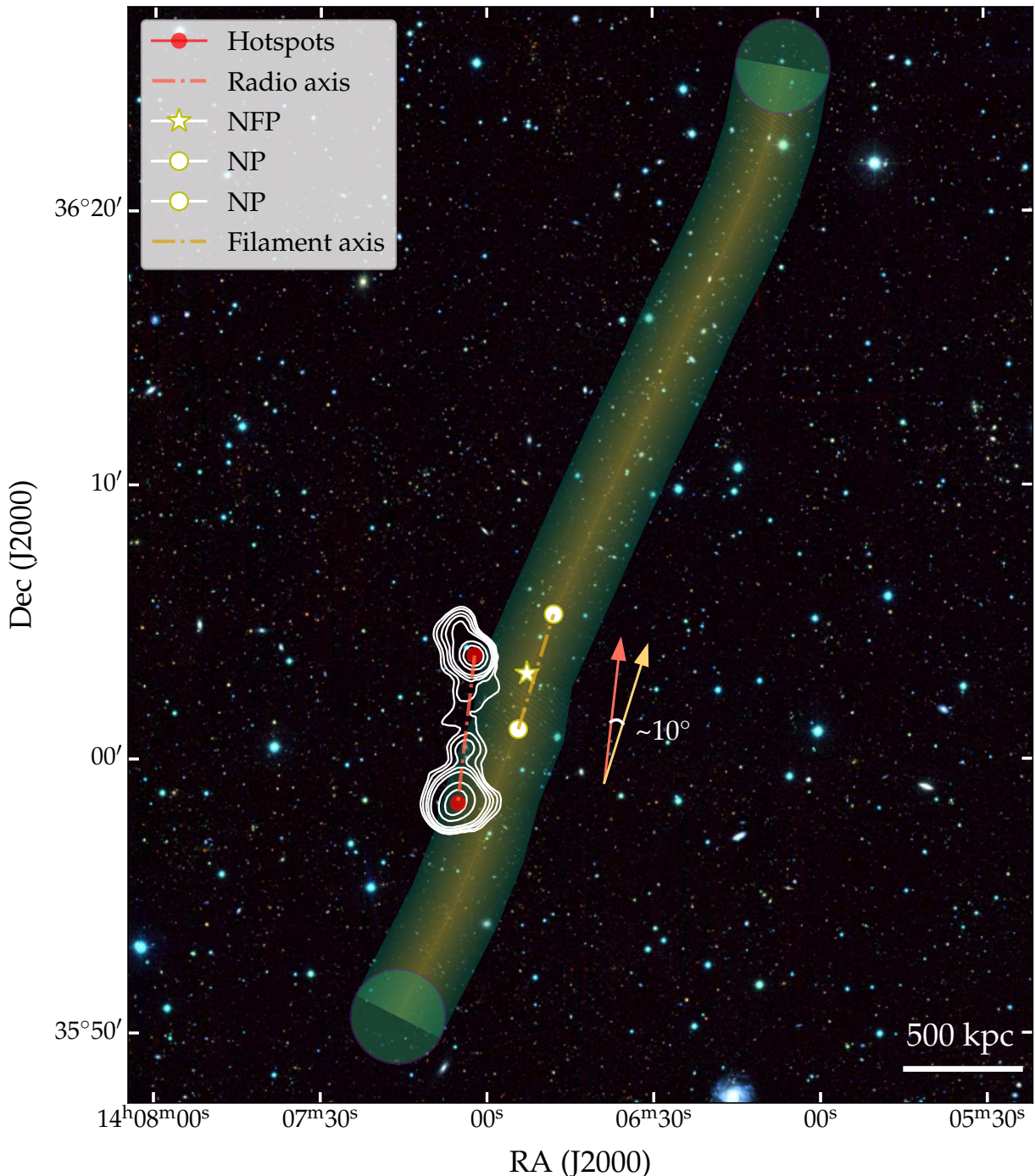


Fig. A.1: The figure gives the view of GRG (RA:  $211.7667^\circ$ , Dec:  $36.0082^\circ$ ), whose jet axis is nearly parallel to the filament, forming an angle of  $\sim 10^\circ$  with the filament axis. A green cylindrical spine traces the inner 400 kpc of the nearest filament; the nearest filament point (NFP) is indicated by a yellow star, and neighbouring points (NP) are shown as white circles. The white NVSS (beam =  $45''$ ) 1400 MHz radio contours above  $3\sigma$  ( $\sigma \sim 0.45 \text{ mJy beam}^{-1}$ ) are overlaid on the Legacy Surveys optical RGB image. The hotspots are marked by red circles. The red and yellow dashed lines indicate the radio and filament axes, respectively. Arrows of the same colours are drawn parallel to their axes. The angle between the two arrows quantifies the alignment of the GRG with the filament on the plane of the sky.

## Appendix A: Images

Here, we present optical RGB images from the Legacy survey overlaid with radio contours from radio surveys, along with filaments outlined.

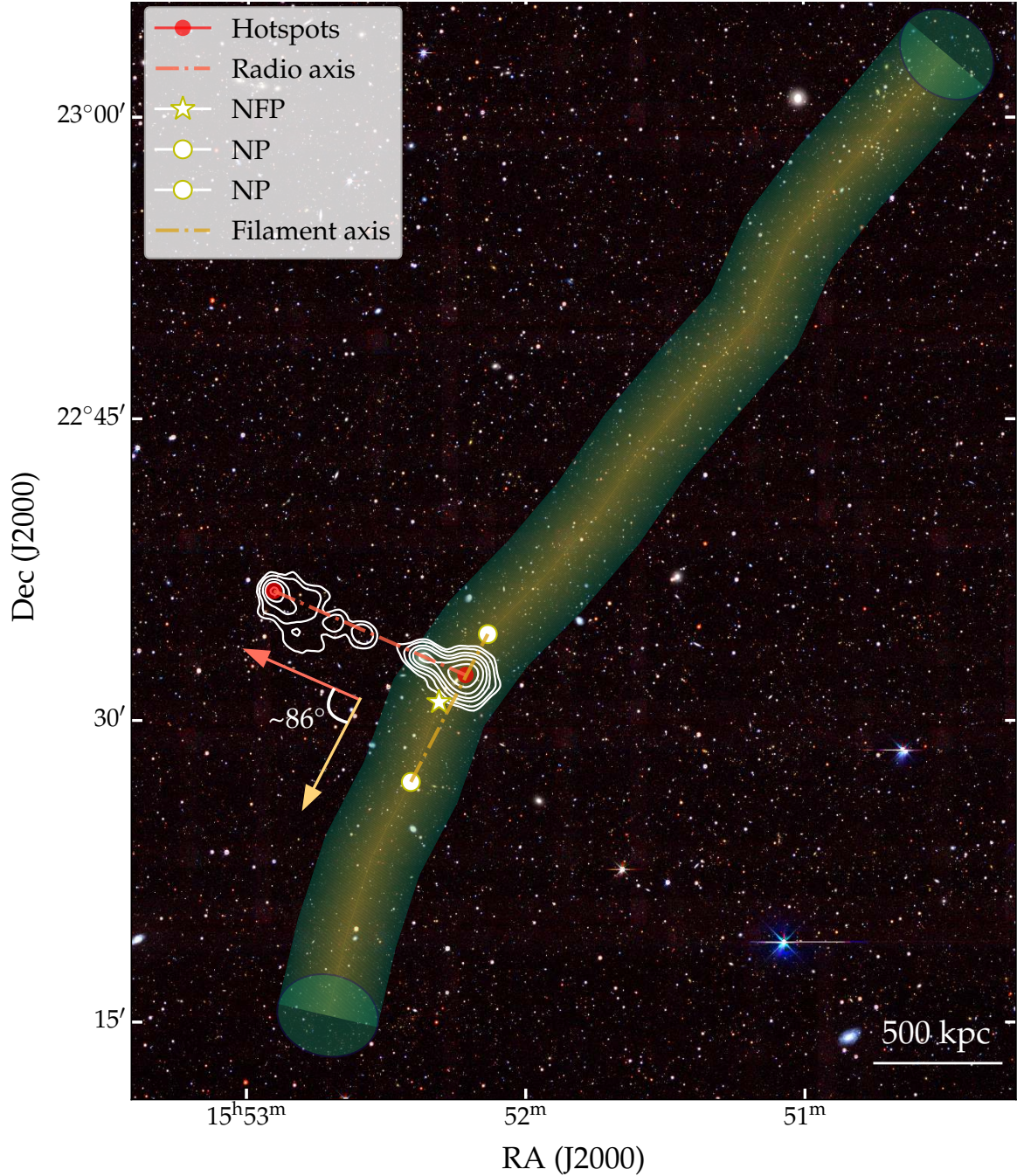


Fig. A.2: Same plotting conventions as in Fig. A.1. This figure shows the GRG at RA:  $238.0931^\circ$ , Dec:  $22.5533^\circ$ . White NVSS 1400 MHz contours (beam =  $45''$ ,  $\sigma \sim 0.45 \text{ mJy beam}^{-1}$ ) above  $3\sigma$  are overlaid on the Legacy Surveys RGB image. The nearest filament is traced over its inner 400 kpc, the yellow star marks the NFP with neighbouring points (NP) indicated by white circles. The GRG jet axis is nearly perpendicular to the filament, forming an angle of  $\sim 86^\circ$  with the filament axis. Red circles denote the hotspot positions. The radio axis and filament axis are shown by red and yellow dashed lines, respectively, with the same coloured arrows drawn parallel to each. The angle between the two arrows measures the alignment of the GRG with the filament on the plane of the sky.

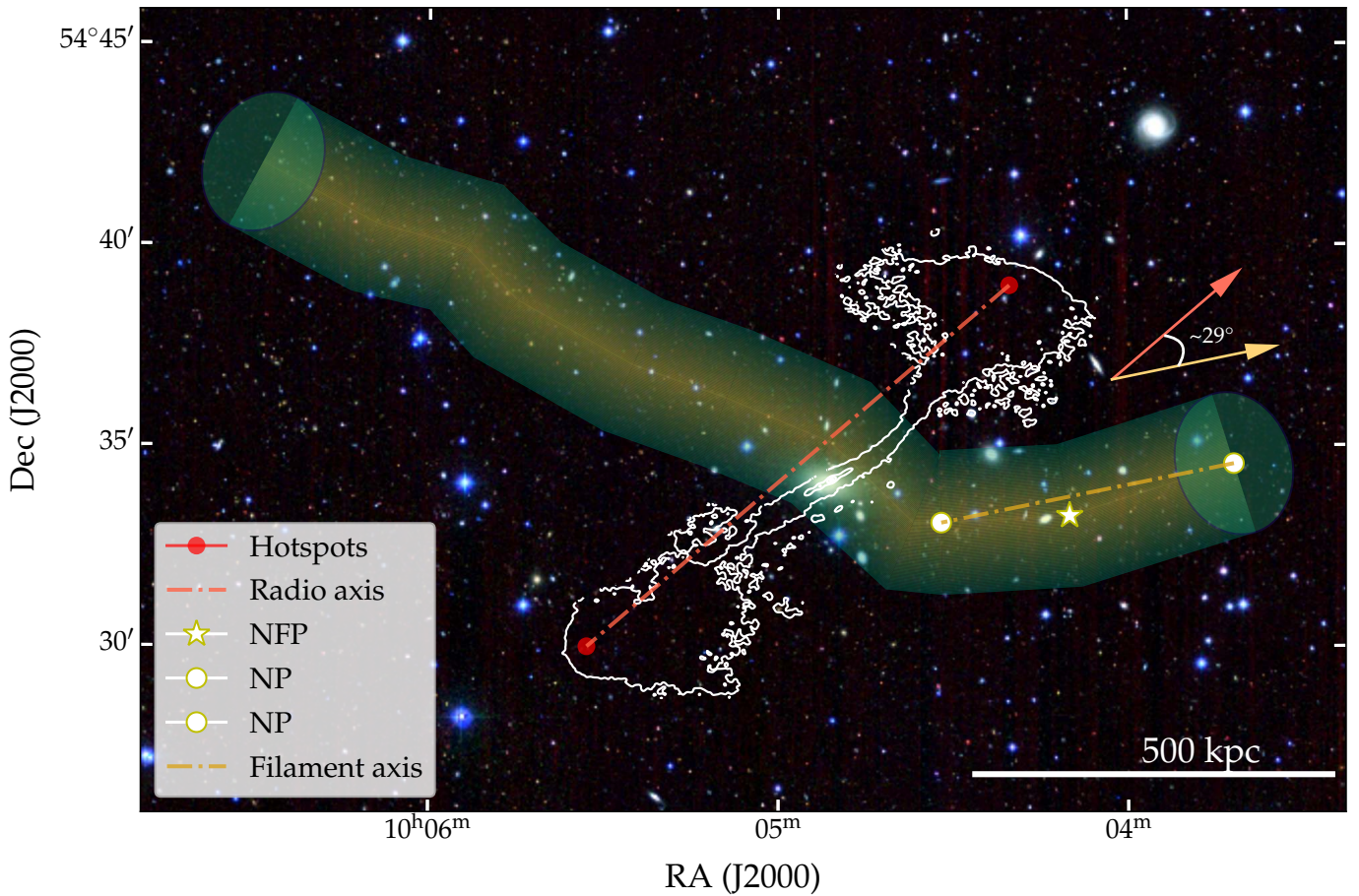


Fig. A.3: As in Fig. A.1 but for the GRG at RA:  $151.2168^\circ$ , Dec:  $54.5678^\circ$ . Here, the radio map is from LoTSS at 144 MHz with a  $6''$  beam, shown as white contours above  $3\sigma$  ( $\sigma \sim 50 \mu\text{Jy beam}^{-1}$ ). The filament spine is traced over its inner 200 kpc, the yellow star marks the NFP and its neighbouring points (NP) are plotted as white circles. The GRG jet axis forms an angle of  $\sim 29^\circ$  with the filament axis. Red circles mark the hotspot positions. The background is the Legacy Surveys optical RGB image of the sky. The dashed lines indicate the radio (red) and filament (yellow) axes; corresponding red and yellow arrows are drawn parallel to them. The angle between the arrows represents the GRG-filament alignment on the plane of the sky.

## Appendix B: Table

As described in Sec. 3.1, here we list the samples of GRGs and SRGs with their properties.

Table B.1: Properties of FRII GRGs and SRGs in cosmic web filaments. Columns (2) & (3) represent the right ascension (RA) and declination (Dec) in degrees of the host galaxies of the GRGs and SRGs. Column (4) lists the spectroscopic redshifts of the hosts. Column (5) lists the projected linear sizes of the sources in Mpc. Columns (6), (7), (8) & (9) respectively, state the RA and Dec of two hotspots. Columns (10) & (11) contain the 3D distances of GRGs and SRGs from their local filaments, and their orientations with them. Column (12) gives the measurements of their arm-length ratios.

No	RA (deg)	Dec (deg)	$z$	Size (Mpc)	RA: HS1 (deg)	Dec: HS1 (deg)	RA: HS2 (deg)	Dec: HS2 (deg)	$D_{\text{fil}}$ (Mpc)	Alignment (deg)	ALR
(1)	(2)	(3)	(4)	(5)	(6)	(7)	(8)	(9)	(10)	(11)	(12)
GRG											
1	116.0338	43.9917	0.13484	0.73	116.0360	44.0212	116.0240	43.9600	1.5	84.2	0.91
2	118.1446	35.8398	0.13650	2.34	118.1587	35.8580	118.1369	35.8150	3.2	54.0	0.84
3	119.1594	32.4631	0.14620	1.29	119.2373	32.4730	119.1061	32.4435	0.8	89.8	0.74
4	127.8645	32.3241	0.05120	0.79	127.8243	32.3065	127.9014	32.3418	2.2	47.3	0.94
5	127.9987	30.6585	0.10704	2.28	128.0388	30.7812	127.9561	30.4930	0.8	74.3	0.75
6	129.0320	26.8121	0.08780	1.00	129.1003	26.8027	128.9730	26.8143	0.5	23.7	0.85
7	131.2433	42.0774	0.14932	1.70	131.2454	42.0785	131.2399	42.0759	0.2	80.9	0.64
8	131.3629	44.9240	0.15062	0.81	131.3403	44.9638	131.3691	44.9022	0.4	46.7	0.52
9	134.8236	63.7514	0.12010	0.83	134.8774	63.7794	134.7889	63.7018	0.8	61.4	0.71
10	139.9519	57.8489	0.13695	0.72	139.9678	57.8496	139.9303	57.8535	1.1	12.4	0.69
11	140.8813	24.4463	0.03452	0.77	140.8565	24.5825	140.9423	24.3533	2.5	58.4	0.79
12	143.5899	38.3849	0.12299	0.72	143.5735	38.4254	143.6050	38.3559	0.4	67.5	0.74
13	144.6027	64.7014	0.13881	1.06	144.5699	64.6916	144.6394	64.7099	0.2	49.2	0.96
14	146.7867	42.1904	0.07213	0.81	146.7623	42.1707	146.8467	42.2347	1.7	38.5	0.43
15	149.9183	17.4245	0.12347	1.21	149.9442	17.4969	149.8784	17.3565	0.3	44.3	0.98
16	151.2168	54.5678	0.04701	0.89	151.0845	54.6498	151.3869	54.5000	0.4	29.1	0.94
17	151.5073	34.9029	0.09936	4.88	151.9172	34.6816	151.2578	35.0336	1.3	78.1	0.60
18	151.5984	24.0906	0.07517	0.92	151.5922	24.1003	151.5968	24.0739	1.2	6.5	0.67
19	154.8433	32.1561	0.09583	0.72	154.9022	32.1474	154.7916	32.1669	1.3	75.9	0.89
20	155.3509	12.2848	0.12938	2.32	155.4510	12.3291	155.2553	12.2072	4.5	49.4	0.88
21	156.3216	48.5371	0.14920	1.36	156.2364	48.5520	156.4044	48.5245	2.3	60.3	0.97
22	158.0586	27.9333	0.08540	1.09	158.0514	27.9926	158.0719	27.8265	1.0	14.8	0.55
23	162.7187	40.0141	0.12947	0.95	162.6950	40.0150	162.7521	40.0152	2.6	40.6	0.71
24	169.9331	13.9639	0.06874	1.14	169.8981	14.0032	169.9755	13.9452	0.8	64.4	0.87
25	171.8767	17.1266	0.12973	1.15	171.8518	17.1310	171.9284	17.1218	0.3	84.7	0.49
26	176.1133	37.1422	0.11482	0.86	176.0804	37.1172	176.1442	37.1714	1.2	82.8	0.95
27	176.8420	35.0187	0.06289	0.91	176.9539	34.9909	176.7518	35.0280	1.4	68.0	0.78
28	183.8924	13.9430	0.09341	0.82	183.8401	13.9322	183.9442	13.9429	1.1	50.8	0.97
29	186.5938	64.1061	0.11024	0.88	186.5809	64.0928	186.6699	64.1397	2.3	70.9	0.31
30	189.4413	-1.2378	0.13531	1.72	189.4322	-1.1382	189.4434	-1.2673	0.3	22.1	0.30
31	198.0707	44.8393	0.03580	1.00	198.3296	44.8310	197.7798	44.8510	1.8	78.3	0.89
32	202.1432	-3.1291	0.08525	1.33	202.1944	-3.0214	202.1051	-3.2260	2.2	56.7	0.87
33	211.7667	36.0082	0.10475	0.93	211.7593	36.0632	211.7718	35.9735	0.5	10.7	0.63
34	217.0800	29.3123	0.08699	1.72	217.1680	29.3891	216.9565	29.2190	1.6	79.1	0.76
35	218.2409	4.6209	0.10552	0.79	218.2259	4.5972	218.2817	4.6588	2.0	38.4	0.50
36	221.3642	9.5383	0.09448	0.78	221.3243	9.5339	221.4049	9.5409	1.7	38.5	0.98
37	223.6808	12.4196	0.12199	0.94	223.6597	12.4347	223.7185	12.4034	1.3	17.6	0.64
38	225.1311	36.4805	0.09256	1.45	225.1233	36.4833	225.1395	36.4775	1.2	62.8	0.93
39	225.2641	51.9671	0.13210	0.79	225.1911	51.9816	225.3009	51.9710	1.6	74.8	0.49
40	226.8555	8.4957	0.07867	0.77	226.8432	8.5091	226.8915	8.4469	1.8	77.3	0.30
41	227.4985	3.0010	0.09234	1.09	227.4847	2.9731	227.4993	3.0357	2.8	41.4	0.90
42	231.5492	29.6513	0.11664	1.79	231.5836	29.7171	231.5813	29.4925	1.2	65.4	0.45
43	238.0278	22.7943	0.11540	1.70	238.0168	22.8216	238.0665	22.6741	1.4	77.6	0.23
44	238.0383	20.0897	0.08950	2.08	238.1020	20.0863	237.8380	20.0530	0.8	15.3	0.31
45	238.0931	22.5533	0.06831	0.98	238.2262	22.6076	238.0541	22.5381	0.7	86.2	0.29
46	250.9306	32.5790	0.13525	1.17	250.8928	32.5756	250.9858	32.6105	0.6	75.6	0.57
SRG											
1	120.4920	17.8646	0.14700	0.09	120.4966	17.8663	120.4876	17.8633	0.3	35.3	0.96
2	123.8014	38.6793	0.12500	0.08	123.8018	38.6830	123.8025	38.6739	1.2	81.3	0.68

Table B.1: continued.

No	RA (deg)	Dec (deg)	$z$	Size (Mpc)	RA: HS1 (deg)	Dec: HS1 (deg)	RA: HS2 (deg)	Dec: HS2 (deg)	$D_{\text{fil}}$ (Mpc)	Alignment (deg)	ALR
(1)	(2)	(3)	(4)	(5)	(6)	(7)	(8)	(9)	(10)	(11)	(12)
3	125.6985	4.2972	0.09500	0.14	125.7078	4.2929	125.6884	4.3024	3.4	47.4	0.90
4	139.9519	57.8489	0.13700	0.37	139.9707	57.8497	139.9299	57.8540	1.2	12.3	0.79
5	141.5469	17.0661	0.11600	0.08	141.5501	17.0626	141.5431	17.0698	4.0	73.9	0.88
6	145.3501	39.7449	0.10800	0.16	145.3536	39.7554	145.3466	39.7352	2.0	53.7	0.93
7	145.5073	8.7936	0.13400	0.16	145.5155	8.7941	145.4975	8.7934	3.5	23.5	0.84
8	146.7625	23.2706	0.08400	0.11	146.7581	23.2783	146.7652	23.2618	0.3	34.7	0.95
9	153.9927	40.7798	0.12800	0.39	154.0132	40.7841	153.9673	40.7773	3.5	20.4	0.83
10	154.9770	39.5063	0.11200	0.25	154.9682	39.5185	154.9895	39.4932	1.2	38.2	0.86
11	155.4861	14.7254	0.11100	0.25	155.4970	14.7370	155.4747	14.7130	0.4	82.6	0.94
12	161.2614	47.2998	0.14500	0.09	161.2665	47.3000	161.2573	47.2993	0.4	49.2	0.82
13	161.9285	43.7813	0.08600	0.19	161.9416	43.7932	161.9162	43.7751	0.4	36.8	0.71
14	162.7186	40.0141	0.12900	0.50	162.7534	40.0142	162.6949	40.0138	0.7	41.9	0.68
15	165.1462	25.6531	0.14500	0.14	165.1428	25.6608	165.1494	25.6471	2.9	24.1	0.80
16	168.3246	41.4081	0.09500	0.31	168.3101	41.4158	168.3516	41.3934	1.5	63.9	0.53
17	172.8899	60.7911	0.14500	0.06	172.8910	60.7891	172.8865	60.7940	1.7	86.2	0.61
18	174.1098	50.2233	0.05400	0.08	174.1182	50.2169	174.1033	50.2301	0.8	22.3	0.96
19	176.1133	37.1422	0.11500	0.65	176.1444	37.1716	176.0805	37.1173	1.8	64.4	0.94
20	176.1171	3.9710	0.12700	0.08	176.1206	3.9717	176.1118	3.9693	2.5	36.6	0.64
21	177.4505	43.9035	0.07100	0.07	177.4534	43.9119	177.4491	43.8983	0.2	61.0	0.62
22	178.8550	25.5396	0.13700	0.08	178.8522	25.5427	178.8588	25.5360	4.3	59.8	0.81
23	181.8872	33.8778	0.07900	0.08	181.8805	33.8823	181.8923	33.8742	0.9	61.4	0.78
24	185.2185	31.5523	0.10400	0.06	185.2148	31.5553	185.2212	31.5504	1.5	39.7	0.69
25	198.7910	8.6815	0.09300	0.38	198.7985	8.7109	198.7845	8.6530	0.6	13.6	0.96
26	200.3242	42.5876	0.07900	0.34	200.3536	42.5874	200.2933	42.5799	2.3	60.2	0.90
27	207.8245	64.1603	0.10900	0.16	207.8355	64.1617	207.8143	64.1594	0.9	24.9	0.89
28	213.8634	17.4086	0.12400	0.06	213.8645	17.4124	213.8621	17.4057	4.4	25.0	0.82
29	222.4538	33.8574	0.08800	0.11	222.4477	33.8666	222.4574	33.8516	1.5	43.1	0.63
30	224.4742	28.5385	0.14400	0.56	224.4926	28.5609	224.4561	28.5140	0.2	85.8	0.94
31	227.1138	54.2521	0.09600	0.11	227.1230	54.2511	227.1070	54.2537	0.6	42.4	0.79
32	229.1675	0.2505	0.05300	0.26	229.1445	0.2715	229.1937	0.2267	1.4	71.4	0.88
33	230.6900	19.7056	0.10900	0.06	230.6949	19.7054	230.6871	19.7057	1.2	18.2	0.60
34	230.7391	2.9200	0.11000	0.10	230.7440	2.9155	230.7348	2.9243	1.3	25.5	0.90
35	239.7194	26.4386	0.08700	0.23	239.7098	26.4585	239.7263	26.4237	1.3	37.3	0.74

### Appendix C: Uncertainty estimation for radio jet axis position angle

To estimate the uncertainties in our measurements of the radio jet axis position angles, we adopt the standard formalism of [Condon \(1997\)](#) and [Fomalont \(1999\)](#). For an unresolved or compact hotspot observed with a Gaussian restoring beam, the uncertainty in its centroid position is given by:

$$\sigma_{\text{pos}} \approx \frac{\text{FWHM}}{2 \text{SNR}_{\text{peak}}}$$

where FWHM is the full width at half maximum of the beam, and SNR<sub>peak</sub> is the peak signal-to-noise ratio of the hotspot. In our calculations, we adopt SNR<sub>peak</sub> = 3 as a conservative lower limit when estimating centroid uncertainties. Since the radio jet axis is defined by the line joining the two hotspots, the positional uncertainties of both hotspots contribute to the error in the measured position angle ( $\sigma_{\theta}$ ). Propagating these uncertainties yields:

$$\sigma_{\theta} \approx \frac{\sqrt{2}\sigma_{\text{pos}}}{L} \quad (\text{radians})$$

Here,  $L$  (in arcsec) is the hotspot-hotspot separation, i.e., the projected angular size of the GRG. Using the median angular size of our sample ( $L = 9.67'$ ) and adopting SNR<sub>peak</sub> = 3, we obtain position-angle uncertainties of  $\sigma_{\theta} \approx 0.93^\circ$  for the LOFAR low-resolution images (144 MHz, FWHM = 20'') and  $\sigma_{\theta} \approx 0.28^\circ$  for the LOFAR high-resolution images (144 MHz, FWHM = 6''). For the FIRST (1400 MHz, FWHM = 5'') and NVSS (1400 MHz, FWHM = 45'') images, the corresponding uncertainties are approximately 0.23° and 2°, respectively. Thus, the radio jet axis uncertainties in our measurements are typically well below 1°, and are far too small to influence the statistical results or the interpretation of the orientation analysis.